2.14 Comparisons between observed and predicted transports.

We have described a number of deep straits and sills (Figure I4) that act as potential sites of hydraulic control and, therefore, as choke points in the lower limbs of the ocean conveyor. At the time of this writing, comparisons between the observed features of these overflows and inviscid hydraulic models were based largely on volume transport (or flux). The lack of measurements with sufficient coverage to resolve boundary currents, and other features of the flow upstream of their sills, has precluded detailed comparisons with models such as Gill (1977). We do not, for example, have a good understanding of how well the reservoir states postulated by Whitehead, et al (1974, hereafter WLK), Gill (1997), Killworth (1992) and Pratt (1997) agree with reality. Nevertheless, comparisons of observed and predicted transport are important, not only as a test of the models but also as a step towards the development of strategies for monitoring the ocean thermohaline circulation.

The most common transport (or 'weir') formula in current use is that due to WLK. As shown in Section 2.4, the volume flux across the sill is given by

$$Q_0{*} = \frac{g'(\Delta z{*})^2}{2f} \qquad \text{if} \quad w{*}_c \geq \frac{\sqrt{2g'\Delta z{*}}}{f}, \tag{2.14.1a}$$

or

$$Q_0{*} = \left(\frac{2}{3}\right)^{3/2} w_c{*}\sqrt{g'}\left[\Delta z{*} - \frac{w_c{*}^2 f^2}{8g'}\right]^{3/2} \qquad \text{(otherwise).} \tag{2.14.1b}$$

The symbol Q_0 for volume transport is used here as a reminder that the 'zero potential vorticity' approximation is in effect. Also, the reduced form of the gravitational acceleration $g'=g\Delta\rho/\rho$, $\Delta\rho=\rho-\rho_1$, is explicitly used to acknowledge application to an overflowing layer of density ρ that underlies an inactive layer of density ρ_1. The interface separating the two layers is usually chosen to correspond to a particular isopycnal. The transport then depends on the elevation difference $\Delta z*$ between the sill and the upstream interface. The geometry of the sill section is assumed to be rectangular and the upstream interface is assumed to be horizontal. In reality, the choices of the bounding isopycnal and its upstream level, the layer densities, and the elevation and width w_c* at the sill section, require a number of *ad hoc* assumptions. Once $\Delta z*$ is estimated, a choice is made between the first and second formulae corresponding to separated and attached sill flow. We later describe a systematic method for estimating the parameters.

Several features make the WLK model a good starting point for comparison. First, it is based on the simplist of models and therefore requires the fewest parameters. More sophisticated models such as Gill's (1977) require additional upstream information that may or may not be available. Also, as explained in Section 2.6, the formula (2.14.1) is valid for a wide class of flows with arbitrary potential vorticity, provided that the flow is separated at the sill and that $\Delta z*$ is measured along the right wall of the upstream basin. The same formula also gives a bound on flow on inviscid, rotating channel flow across a sill of arbitrary topography, provided that $g'\Delta z*$ is interpreted as the maximum value of the Bernoulli function over streamlines in the upstream basin that cross the sill.

The WLK model formally depends on an assumption that is difficult to justify. In particular, fluid columns must able to make their way from a hypothetical deep and quiescent basin up over a shallow sill. It is well know that slow, nearly geostrophic motion on an *f*-plane resists such changes: the fluid columns tend to move along, not across, isobaths. In the ocean, it is more likely the case that fluid passing over a deep sill originates from an upstream layer that lies at an intermediate depth and is suspended above the bottom. Fluid below this layer is blocked from passing across the sill. The layer thickness over the sill is no longer much greater than the upstream thickness and the zero potential vorticity approximation no longer holds. The Gill (1977) or Killworth (1992) models, in which the potential vorticity is finite, are now more appropriate[1].

Several attempts have been made to use uniform potential vorticity models such as that of Gill (1977) and extensions to non-rectangular sill geometries. Prediction of the flux requires that the a represenative value of the potential vorticity of the overflow must be measured and this is not always possible. In the examples we shall cite, the potential vorticity is often unknown. However, it is still possible to estimate the importance of the effect of finite potential vorticity on the transport. To this end, consider the case in which the nondimensional potential vorticity q is equal to unity. For the theory developed in Section 2.6 this means

$$q = \frac{g'^{-1}B_R* - h_c*}{D_\infty} \ ,$$

where B_R* is the value of the Bernoulli function on the right wall and h_c* is the elevation of the sill above the flat bottom. The transport for q=1 is then given by (6.2.7) as

$$Q_1* = \frac{g'(\Delta z_R*)^2}{f} Q(1, w_c*), \qquad (2.14.2a)$$

and the function $Q(1,w_c*)$ can be approximated as

$$Q(1,w_c) = 0.5 - 0.6331e^{-1.45w_c} + 0.1331e^{-2.9w_c} \qquad (2.14.2b)$$

to within a error less than 1.3%. The dimensionless sill width is defined as $w_c = fw_c*/(B_R* - g'h_c)$ and thus it is necessary to measure the right-wall Bernoulli function to compute the transport. Although it is difficult to measure B_R* in practice, there is a special case for which it reduces to $g'\Delta z$*. Suppose that overflow is fed from an intermediate layer as described above and suppose that all fluid below the sill level is blocked. That is, the isopycnals that bounds the intermediate layer below lies right at the sill level. This situation is equivalent to setting h_c* in the above theory to zero, so that $gD_\infty = B_R$*. It can further be shown that the boundary current that enters the strait from the basin does so entirely along the left wall, so that the right wall layer thickness equals the interior thickness D_∞. Also, because the sill height is zero, $D_\infty = \Delta z$*, and thus B_R*$=g'\Delta z$*. In this case

[1] A slight adjustment would have to be made in how the upstream conditions are viewed. Inthe Gill (1977) model, which assumes flow over a horizontal bottom, the value of g' would have to be changed to that relevant for a suspended layer.

$w_c = fw_c^*/g'\Delta z^*$ and the transport depends only on Δz^*. With these approximations, Q_1^* may be interpreted as a benchmark transport for finite potential vorticity. It is the transport for q=1 that occurs when the sill height it zero. Q_1^* will be compared with Q_o^* in order to gain some measure of the sensitivity of the flux to the potential vorticity.

There are many reasons why formule like (2.14.1 or 2.14.2) could fail. Among the most worrisome liabilities are the neglect of friction and time dependence, and the restriction to rectangular geometry. A few recent studies have been able to account for more realistic sill geometries and these will be mentioned below. The effects of friction are much more difficult to deal with. The presence of a bottom Ekman layer and possible frictional layers along a sheared interface lead to energy dissipation and, as shown in Section 2.12, secondary circulations transverse to the channel axis. Johnson and Sanford (1992) report on observations suggesting such features in the Faroe-Bank Channel. The secondary circulations are demonstrated by Johnson and Ohlsen (1994) in a laboratory experiment. Development of a hydraulic transport relation that takes account of these effects has proved elusive.

The issue of time-dependence is also problematic. The hope of steady models is that actual time variations are slow enough to allow the model to be valid at any given instant. There are examples where this is clearly not the case. In fact, awareness of rapid fluctuations dates back to an early current meter deployment at the Denmark Strait (Worthington 1969). Despite massive loss of instrumentation, one current meter recorded large bursts of overflow water, with velocities up to 1.4 m/s and with time scales as short as one day. Other overflows are strongly episodic and can switch on and off or meander back and forth across a moored instrument. McCready et al. (1999) report that the deep flow through the Anagada-Jungern passage can behave this way, with about 10 episodes per year. Variation over longer time scales is also common. The flow across the Ceara Abyssal Plain was found to have a large annual signal and an unresolved interannual component (Hall et al 1997). The latter was later found to be erased after ten years (Limeburner et al. 2005). We have already cited the apparent 50-year trend of decreasing transport in the Faroe-Bank Channel (Figure 2.11.12). In general, one can expect to see time dependence on a variety of scales due to internal waves, tides, mesoscale eddies, interactions with nearby currents, atmospheric forcing, and seasonal and longer scale changes in the surroundings.

For a model to be considered quasi-static, the time scale of variation must be much longer than the time required for a disturbance to propagate the length of the strait. This time is roughly the strait length divided by $(g'D)^{1/2}$. Two-day oscillations in the Denmark Strait do not meet this criterion; 1-2 month variability in Anagada-Jungfern passage probably does.

In cases where the dominant time variability is rapid, the standard practice is to compare the hydraulic prediction with some time-mean transport. The presence of a variety of time scales begs the question of how to measure the mean. We have identified ten locations having current meter data of one month or more**,** which is long enough to average out tides and storms**.** The overflows of the Faroe Bank Channel and the Denmark Strait, which contribute to the formation of North Atlantic Deep Water, are the most thoroughly observed. Five other lie in the path of the northward moving Antarctic Bottom Water in the Atlantic. Starting from the south, they are the Vema Channel, Ceara Abyssal Plain, Romanche Fracture Zone, Vema Gap, and Discovery Gap. The remaining straits include the Anagada-Jungfern Passage, composed of the Grappler Channel and Anagada Passage, which provide the deepest inflows into the Caribbean Basin to supply deep water. Also included is the Samoa Passage in the tropical Pacific, where Antarctic Bottom water moves northward into the Pacific.

Flux estimates using (2.14.1) or (2.14.2) require the values Δz^*, g' and w_c^*, and Whitehead (1989) has suggested a systematic method of computing these quantites. The method makes use of density profiles taken upstream and downstream of the strait in question. As an example, we use two profiles measured in the upstream and downstream basins of the Samoa Passage (Figure 2.14.1). Densities are similar at above 3950 but differ below this depth, ostensibly as a result of the mixing and redistribution of density due to the overflow. Below the 'bifurcation' depth, the split extends to below the Samoa passage sill at approximately 5000 meters. The tendency for the upstream and downstream profiles to split is observed for the 10 straits under consideration, and is represented in Figure 2.14.2 by a generic profile pair. The 'interface' bounding the overflowing layer is selected to coincide with isopycnal that lies at the bifurcation depth in the upstream basin. The bottom cross-section at the sill is plotted next to the profiles. The deepest point is selected to be the sill depth and Δz^* is chosen as the difference between the bifurcation depth and the sill depth. The value of $\Delta\rho$ is chosen as the difference in density between the two profiles at sill depth. For the Samoan Passage, we estimate values $\Delta z^* = 1050\,\text{m}$ and $\Delta\rho = 3\times10^{-5}$ gm/cm^3. The channel width $w_c{}^*$ is defined as the width of the cross-section at the bifurcation depth and is 240km for the Samoan Passage. Finally, the local Coriolis parameter is given by $f = 2\Omega\sin\vartheta$ where ϑ is the latitude of the sill. The volume flux values based on (2.14.1) and (2.14.2), and using the 'bifurcation' method, for all ten examples are listed in Table 2.14.1. All except the Grappler passage correspond to values listed in Table 1 of Whitehead (2005). Original bifurcation figures are in Whitehead (1989) and Whitehead (1998) except for the Anagada and Grappler Passages.

Attempts to improve the accuracy of (2.14.1) have concentrated on more realistic topography and on the effect of non-zero potential vorticity. The outcomes (Table 2.14.2) suggest that the later is not as important as the former. Realistic topography often, but not always, leads to a decrease in the predicted transport and this decrease can be substantial. This tendency is suggested in the work of Börenas and Lundberg (1986, 1988) for flow in a channel of parabolic section. As discussed in Section 2.8, the predicted transport depends on the parameter $r = f^2 / g'\alpha$, where α is the bottom curvature. Sections with large curvature act more like rectangles and departures from this shape therefore become more pronounced as r increases. For zero potential vorticity, it can be shown (equation 2.8.10) that a reduction in transport relative to the rectangular case occurs in proportion to $r^{-1/2}$. The reduction is due largely to the presence of counterflow at the right side of the sill section, which occurs for $r>2/3$. Among the notable case studies is Killworth (1992), who fit rectangular, V-shape, and parabolic cross sections to sills in four passages. For the Denmark Strait and Faroe-Bank Channel, a reduction by factor 4 or 5 in predicted flux is found for the parabola and V-shape relative to the rectangle. Finite potential vorticity effects are found to be much weaker. Börenas and Nikolopoulos (2000) investigate the Jungfern Passage using a model that takes into consideration various shapes, including a close fit to the real sill topography. Reductions in flux relative to the rectangular case are by a factor or 2 or 3. A small amount of reverse flow is also predicted at the sill for the real topography. The predicted transport is slightly raised when this counterflow is excised. Nikolopoulos et al. (2003) apply a similar technique to the Denmark Strait. For the actual sill geometry, a reduction in transport by a factor of 2 relative to a rectangle is found. However, the counterflow is much stronger and a flux value close to the rectangular case is restored when thecounterflow is excised. The effects of finite potential vorticity are again found to be moderate.

These are among the studies summarized on Table 2.14.2. When comparing flux predictions, note that different authors may use different values of $\Delta z*$, g', and w_c* for the same location.

Table 2.14.1. Observed volume transport vs. predictions based on a rectangular sill section.

#	Name	g' 10^{-3} ms^{-2}	$\Delta z*$ m	f 10^{-4} s^{-1}	w_c* km	w_c	Q_0 Sv.	Q_1 Sv.	$Q_{observed}$ Sv.
1	Jungfern Passage	0.45[a]	165	0.45	10	1.65	0.136	0.12	0.085[b]
2	Ceara Abyssal Plain	0.5[a]	430	-0.1	700	15.0	4.62	4.53	2.1[c]
3	Denmark Strait	3.0[a]	580	1.3	350	34.5	3.88	3.8	2.9[d]
4	Discovery Gap	0.1[a]	600	0.87	80	28.4	0.21	0.2	0.21[e]
5	Faroe Bank Channel	5.0[a]	400	1.3	20	1.84	2.82	2.62	1.9[f]
6	Grappler Passage	0.22[b]	160	0.45	-	1.2	0.06		0.026
7	Romanche Fracture Zone	0.73[a]	380	-0.02	20	0.08	2.15	2.09	0.66[g]
8	Samoa passage	0.3[a]	1050	-0.23	240	9.8	7.19	7.05	6.0[h]
9	Vema Channel	1.0[a]	1100	-0.7	446	29.8	8.64	8.62	4.0[i]
10	Vema Gap	0.5[a]	1000	0.28	9	0.36	3.35	3.03	2.1[j]

Note: citations pertain to all information from that citation to the next. Also, negative values of f imply that $|f|$ should be used in the transport formula.

[a] Whitehead 2005

[b] MacCready et al. (1999)

[c] Hall et al(1997)

[d] Dickson, Gmitrowicz and Watson (1990)

[e] Saunders (1987)

[f] Saunders (1990)

[g] Mercier and Speer (1998)

[h] Rudnick (1997)

[i] Hogg, Siedler, and Zenk, (1999)

[j] McCartney et al. (1991)

Table 2.14.2. Observed volume transport vs. predictions based on a non-rectangular sill section.

In the following, 'flat' refers to a rectangle, and 'real' implies a fit to the actual topography. Also note that the observed volume flux $Q_{observed}$ refers to the particular value used for comparison in the study cited. This value depends on the definition of the overflowing fluid and on the time and manner of measurement.

# & Name	Shape	$g*'$ 10^{-3} ms^{-2}	$\Delta z*$ m	w_c* km	w_c	Q *Zero* Sv	Q_1 *other* Sv	$Q_{observed}$ Sv
1.	Flat	0.28[a]	265	6	1.65	0.21		0.085
Jungfern	Flat	0.40[b]	100	5		0.04[d]		0.056
Passage	Flat	0.40[b]	150	6		0.09		0.099
	Real	0.45[b]	165			0.079		0.072
	Real	0.40[b]	150			0.027		0.056
	Real	0.40				0.055		0.099
	RealX[c]	0.45[b]				0.085		0.099
2. Ceara	Flat	0.5[e]	430	700	15.0	4.6		1.1-2.1
Abyssal	Parabola					1.4	2.1	
Plain	V					1.7		
3.	Flat	3.0[e]	580	20		3.8		2.5
Denmark	Parabola					0.5	0.6	
Strait	V					0.7	0.96	
	Flat	4.78[f]	520	20	34.5	4.97		3.7
	Parabola					4.49		
	V					4.33		
	Real					2.32	2.45	
	RealX					4.47	4.35	
	Flat	3.82	370	20		2.01		2.1
	Parabola					1.85		
	V					1.73		
	Real					1.22	1.31	
	RealX					1.83	1.79	
5. Faroe	Flat	5.0[e]	400	20	1.84	3.6		1.9
Bank	Parabola					0.5	0.53	
Channel	V					0.7	0.86	
	Parabola	4.3[h]	350			1.5		1.4
	Parabola		450			2.5		1.9
9. Vema	Flat	1.0[e]	1540	446	29.8	16.4		4.1
Channel	Parabola					2.9	4.5	

	V					3.9	8.8	

Note: citations pertain to all information from that citation to the next.

[a] MacCready et al. (1999)

[b] Borenas and Nikolopoulos (2000)

[c] RealX- the abbreviation for real bottom topography with reverse flow excised

[d] Stalcup, Metcalf and Johnson (1975)

[e] Killworth (1992)

[f] Nikolopoulos, Borenas, Hietala, and Lundberg (2003)

[g] Girton et al (2001)

[h] Borenas and Lundberg (1988)

The flux values in both tables span nearly three orders of magnitude and require a log-log plot to show the entire range (Figure 2.14.3). The volume flux values from Table 2.14.1 for zero potential vorticity and rectangular sill geometry are shown by X-symbols. As expected, the corresponding values lie above the perfect fit diagonal. The values for the finite potential vorticity benchmark (Equation 2.14.2, open circles) lie slightly below the zero potential vorticity values. The greatest difference is approximately 10%, indicating that the value of upstream potential vorticity is not the greatest factor needed to bring the theory into agreement with measurements. In some cases with non-rectangular topography, the finite potential vorticity prediction exceeds that of the zero potential vorticity. The flux values over various bottom shapes (Table 2.14.2) are shown by assorted symbols. For a given strait, variations in the observed flux are indicated by horizontal scatter of like symbols. Variations in predicted fluxes for different geometric fits to the sill topography are indicated by the vertical scatter of different symbols with the same Q_{obs}. The latter is generally larger than the former. Values lying below the diagonal may contain reverse flow, while those lying above have none, or have had the reverse flow excised. Overall, the steady component of flow is bounded by the predictions for flow over a flat bottom, and the influence of bottom shape introduces a wide range of variability in predictions.

Numerical models of overflow regions have received considerable development since about 1990. The numerical schemes attempt to resolve topographic features and eddies on a horizontal scale that is a fraction of the Rossby radius of deformation based on the local depth. Sigma[2] coordinate are often used because of their ability to handle regions with large topographic variations. The models resolve 60 or more levels and are based on primitive equation dynamics. The formulation typically includes parameterizations for both internal mixing and bottom drag.

The earliest studies focus on the dense overflow plume downstream of the sill (Jungclaus and Backhaus 1994, Kraus and Käse 1998, Shi, et al 2001). The lateral scale is smaller than 10 km, allowing partial resolution of fronts and eddies. A second generaltion of models resolves the entire region around the Denmark Strait. In a fully three-dimensional computation by Käse and Oschlies (2000), the computed volume flux agrees within a few tens of percent with (2.14.1). (The value of Δz^* is an depth above the sill of an isopycnal surface, averaged over a region approximately 85km upstream of the sill.) Kosters (2004) compares a number of simple hydraulic estimates to the output

---

[2] 'Sigma' is defined as $(z_T{*}- z^*)/(z_T{*}- h^*)$, where $z_T{*}$ is the elevation of the sea surface. Thus the bottom corresponds to sigma=1.

of a slightly more elaborate numerical model. The model, driven by regional buoyancy forcing, has a lateral grid of 5 km and both idealized and real topography. The hydraulic criticality of the flow is evaluated using several forms of the Froude number, including (2.5.7) for the Gill model. The flow is judged to be critical approximately 80km downstream of the sill. His volume flux comparisons with hydraulic predictions are very similar to those in Table 2.14.2. For example, the zero potential vorticity prediction over a flat bottom is about double the numerical flux. Also, the method from Nikolopoulos and Borenas (2003), using a realistic bottom profile, yields predictions much smaller than the numerical model due to the presence (in the theory) of a return flow. The numerical models generally produce unidirectional flow at the critical section. If the reverse flow predicted by the theory is excised, the prediction comes within 30% of the numerical value. Consistent with the arguments of the previous section, upstream height values progressively closer to the sill produce better predictions.

We have seen that all predictions of the crudest zero potential vorticity theory tend to exceed ocean measurements for volume flux with ratios between one and three. Predictions for parabolic and realistic bottoms can extend below the observed values of flux. A rounded bottom profile sometimes leads to a prediction of return flow at the sill that produces a smaller flux, but excising the return flow increases flux toward flat-bottom values. Overall, it is clear that theory has produced a reasonable bound to observation, but that there is scope for much improvement. A number of aspects could be developed that might lead to improved agreement with observations. These include reconciliation of the issue of counterflow at the sill, and inclusion of time dependence, friction, and continuous stratification.

Figure Captions

Figure 2.14.1. Density (gm/cm ^{3}) corrected to 4000 m depth versus ocean depth at both ends of the Samoa Passage (From Whitehead 1998).

Figure 2.13.2 Ocean data needed to produce values of density, depth and width of a passage.

Figure 2.14.3. Comparison of predicted volume flux to observed volume flux based on values listed in Tables 2.14.1 and 2.14.2. The X-symbols are based on the WLK model (Equations 2.14.1). The large open circles are based on a uniform potential vorticity theory that assumes a sill height of zero and an approach flow entirely along the right wall of the channel (see Equation 2.14.2). The smaller symbols are based on theories that use a non-zero potential vorticity distribution and/or non-rectangular cross sections. Different symbols correspond to different geometries as follows: rectangular cross-section (squares), parabola (small circle), V-shaped bottom (triangle), real bathymetry (plus), and real bathymetry with reversed flow excised (star).

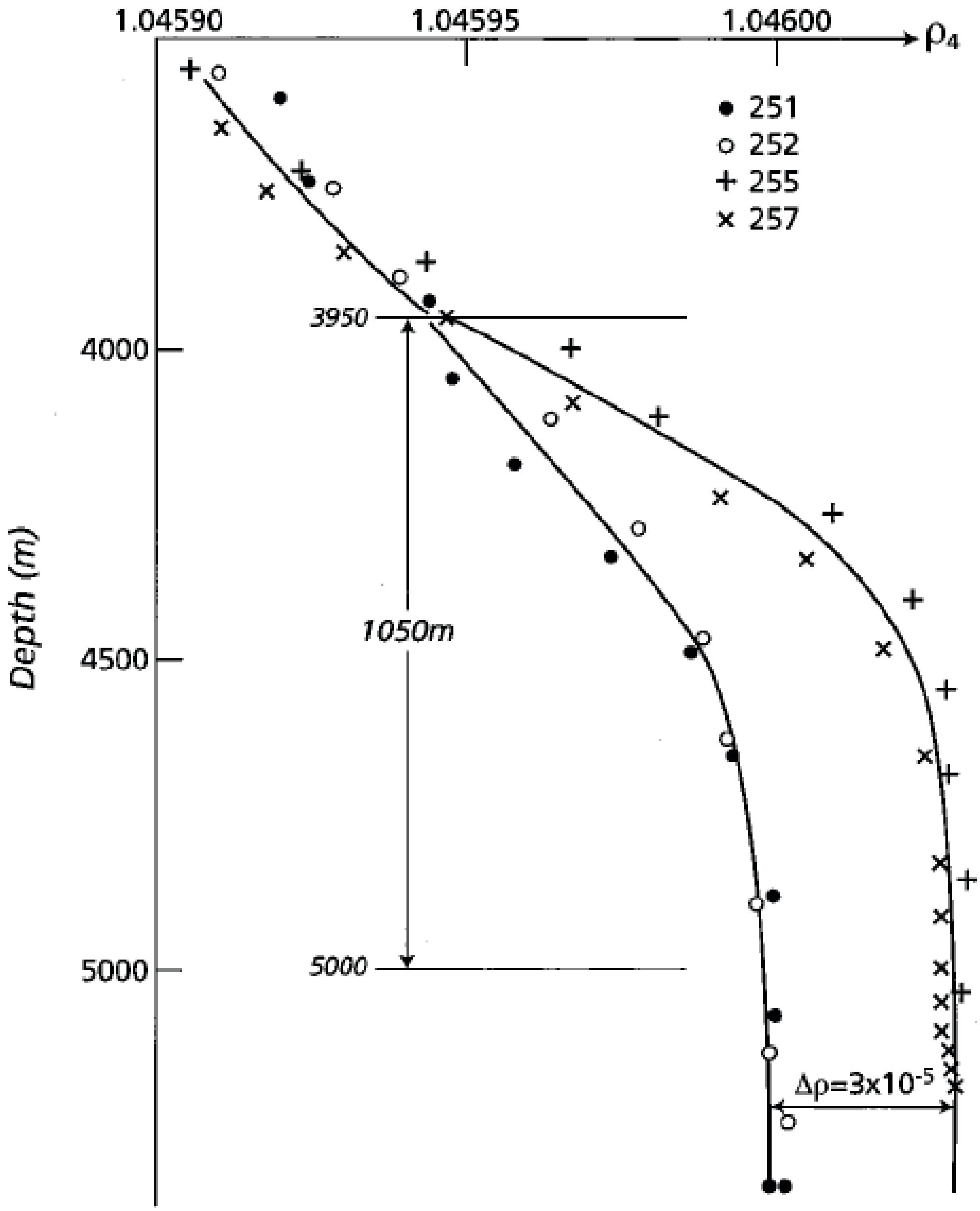
1.04590
1.04595
1.04600
ρ_4
● 251
○ 252
+ 255
× 257
3950
4000
1050m
4500
5000
5000
Depth (m)
$\Delta\rho=3\times10^{-5}$

Figure 2.14.1

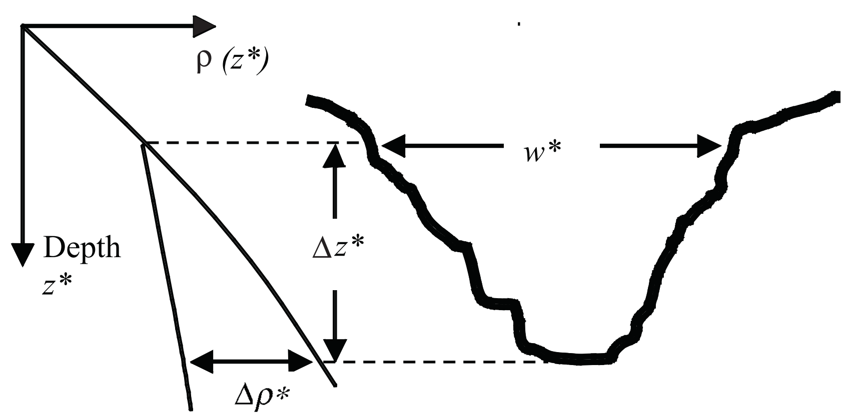

Figure 2.14.2

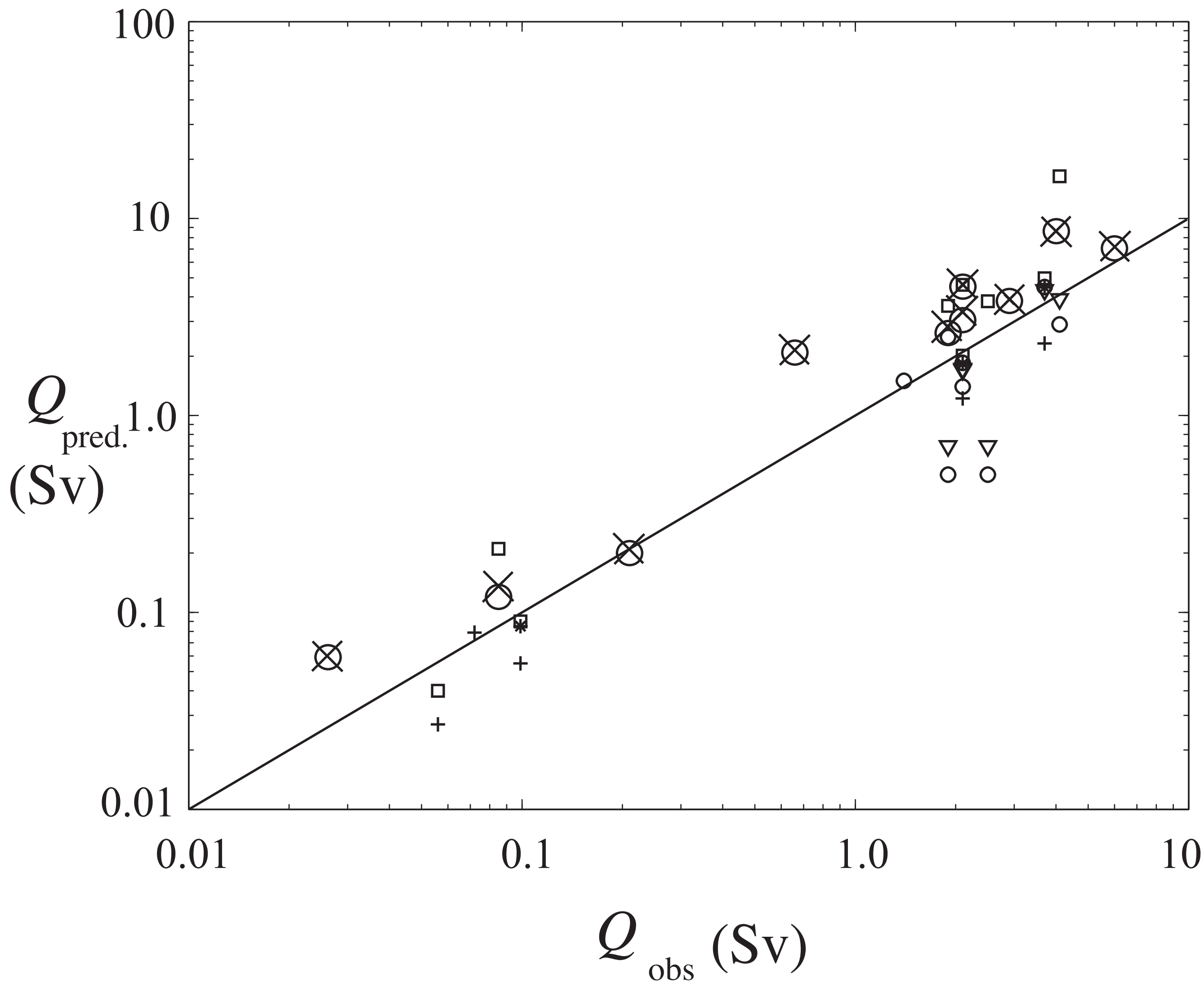

Figure 2.14.3